Kobayashi *Earth, Planets and Space* (2017) 69:7
DOI 10.1186/s40623-016-0594-y

Earth, Planets and Space

LETTER Open Access

Earthquake rupture properties of the 2016 Kumamoto earthquake foreshocks (M_j 6.5 and M_j 6.4) revealed by conventional and multiple-aperture InSAR

Tomokazu Kobayashi*

Abstract

By applying conventional cross-track InSAR and multiple-aperture InSAR (MAI) techniques with ALOS-2 SAR data to foreshocks of the 2016 Kumamoto earthquake, ground displacement fields in range (line-of-sight) and azimuth components have been successfully mapped. The most concentrated crustal deformation with ground displacement exceeding 15 cm is located on the western side of the Hinagu fault zone. A locally distributed displacement which appears along the strike of the Futagawa fault can be identified in and around Mashiki town, suggesting that a different local fault slip also contributed toward foreshocks. Inverting InSAR, MAI, and GNSS data, distributed slip models are obtained that show almost pure right-lateral fault motion on a plane dipping west by 80° for the Hinagu fault and almost pure normal fault motion on a plane dipping south by 70° for the local fault beneath Mashiki town. The slip on the Hinagu fault reaches around the junction of the Hinagu and Futagawa faults. The slip in the north significantly extends down to around 10 km depth, while in the south the slip is concentrated near the ground surface, perhaps corresponding to the M_j 6.5 and the M_j 6.4 events, respectively. The focal mechanism of the distributed slip model for the Hinagu fault alone shows pure right-lateral motion, which is inconsistent with the seismically estimated mechanism that includes a significant non-double couple component. On the other hand, when taking the contribution of normal fault motion into account, the focal mechanism appears similar to that of the seismic analysis. This result may suggest that local fault motion occurred just beneath Mashiki town, simultaneously with the M_j 6.5 event, thereby increasing the degree of damage to the town.

Keywords: Foreshocks, Kumamoto earthquake, InSAR, MAI, Crustal deformation, Fault model

Introduction

A large inland earthquake with a Japan Meteorological Agency (JMA) magnitude (M_j) of 7.3 occurred on April 16, 2016, mainly rupturing the Futagawa fault zone (Fig. 1). Prior to the event, M_j 6.5 and M_j 6.4 events occurred at 21:25 Japan Standard Time (JST) on April 14 and 00:06 on April 15, 2016, respectively. The magnitudes of these events are, as yet, the second and third largest in this series of earthquakes. These events are recognized as foreshocks, considering their temporal relationship with the M_j 7.3 event (Asano and Iwata 2016). The foreshocks are thought to have ruptured the Takano-Shirahata segment of the Hinagu fault zone, which connects with the Futagawa fault zone (HERP 2013) (Fig. 1). The spatiotemporal proximity strongly implies that these events have an intimate relationship with the main shock. Thus, the detailed source properties of the foreshocks could provide fundamental information on why such an earthquake sequence occurred.

It is further noted that a seismic intensity of 7, which is the highest rank in the JMA seismic intensity scale, was recorded at Mashiki town (Fig. 1). Some reasons can be considered for why the damage was so major, reportedly leading to 9 fatalities and over 800 injuries in spite of the

*Correspondence: kobayashi-t96dv@mlit.go.jp
Geospatial Information Authority of Japan, 1 Kitasato, Tsukuba, Ibaraki 305-0811, Japan

magnitude of M_j 6.5 (M_w 6.2). These include bad soil conditions, rupture directivity, building vulnerability. They are all reasonable factors that would increase the damage, but to date, no evidence has definitively shown which factors are dominantly responsible.

An L-band synthetic aperture radar (SAR) satellite, known as the Advanced Land Observing Satellite 2 (ALOS-2), makes observations with an emergency operation for the purpose of detecting crustal deformation using SAR interferometry (InSAR). Although continuous GNSS observation sites (GEONET) are densely deployed in and around the fault zone with an average placement interval of approximately 20 km (Fig. 1), it remains difficult to obtain spatially detailed displacement data for moderate-sized earthquakes, impeding comprehensive analysis of the source properties, such as fault modeling. By contrast, InSAR is capable of detailed mapping of crustal deformation from the foreshocks, which can provide information on the spatial features of the fault rupture.

The primary purpose of this study is to rapidly report the rupture location and style of the foreshocks by retrieving crustal deformation using ALOS-2 data. I first report crustal deformation derived from standard and advanced InSAR analyses and examine the ruptures as a whole, including both the M_j 6.5 and M_j 6.4 events. Next, I construct a fault model to understand the rupture properties and then analyze the possible factors responsible for why Mashiki town suffered such serious damage.

Data and analysis

SAR data and analysis method

JAXA (The Japan Aerospace Exploration Agency) carried out an emergency observation of ALOS-2 on April 15, 2016 (Fig. 1b; Table 1). This is the only image acquired after the foreshocks and before the mainshock, and for this orbit path, there is only one earlier acquisition, on November 14, 2014, that can be used as a master image for the InSAR analysis. Thus, this is the unique data pair that can observe the crustal deformation caused by the foreshocks alone. Incidentally, there were no data available from the Sentinel-1A satellite.

A drawback of InSAR is that no displacement can be measured along the flight direction (azimuth component). The satellite used in this analysis flies parallel to the Hinagu fault zone. According to seismic data analyses, a dextral motion is predominant for both the M_j 6.5 and the M_j 6.4 events (JMA 2016b). Thus, conventional cross-track, line-of-sight (LOS) InSAR (hereafter called InSAR) is insensitive to ground movement near the fault where along-track displacement is expected to dominate. In this context, to derive further information on crustal deformation, I applied multiple-aperture interferometry, generally known as MAI (Scheiber and Moreira 2000; Bechor and Zebker 2006), where the basic method of Barbot et al. (2008) was followed. Although the azimuth component can be measured also by a pixel offset method (Michel et al. 1999; Kobayashi et al. 2009), the measurement accuracy, in general, is worse than that of MAI. This is why I here applied the MAI method. In this method, the frequency band of the already focused SLC data is divided into two parts. This operation creates two SLC images with positive and negative Doppler frequencies, equivalent to forward- and backward-looking images, respectively. Using these sub-aperture images, I made forward- and backward-looking interferograms and then converted the displacement to the azimuth component. I took 32 by 32 looks in both range and azimuth directions, resulting in a pixel spacing of about 46 and 59 m, respectively. I applied the adaptive Goldstein filter (Goldstein and Werner 1998) with a coefficient of 1.0 to improve the coherence.

Long spatial wavelength signals, which are presumably due to ionosphere-related noise, are included in both the InSAR and the MAI results. To remove the noise for the InSAR, a GNSS-based noise reduction was applied, which approximates the method utilized by Tobita et al. (2005). For the MAI, I applied a Gaussian filter to model the long-wavelength noise because the spatial pattern of noise is too complicated to correct using the GNSS-based reduction method.

I reduced the atmosphere-related noise using a numerical weather model for the InSAR data (Kobayashi et al. 2014). For the MAI, most of the atmospheric noise was canceled out between the forward- and backward-looking images; thus, no noise reduction was required. The ALOS-2 data were processed using GSISAR software (Fujiwara and Tobita 1999; Fujiwara et al. 1999; Tobita et al. 1999; Tobita 2003), and the software package GAMMA (Wegmüller and Werner 1997) was used for MAI processing.

I utilized GEONET data to obtain the coseismic displacement vectors for the long-wavelength noise correction and a fault modeling. To obtain the coseismic displacement, I took the difference in coordinate data corresponding to the observation dates of the master and slave images. To derive stable coordinate data for the master image, I took an average of amplitudes (positions) in the time series data for F3 data from November 9, 2014, to November 18, 2014 (10 days). F3 data consist of daily coordinates, which are the most accurate data in the analysis strategy of GEONET. For the slave image, I averaged the time series data of Q3 data, which was calculated every 3 h with a 6-h data window (Nakagawa et al. 2009), from 03:00 to 23:59 (JST). Site 940093 had non-negligible noise in the vertical component, and thus, this site was not used for the modeling.

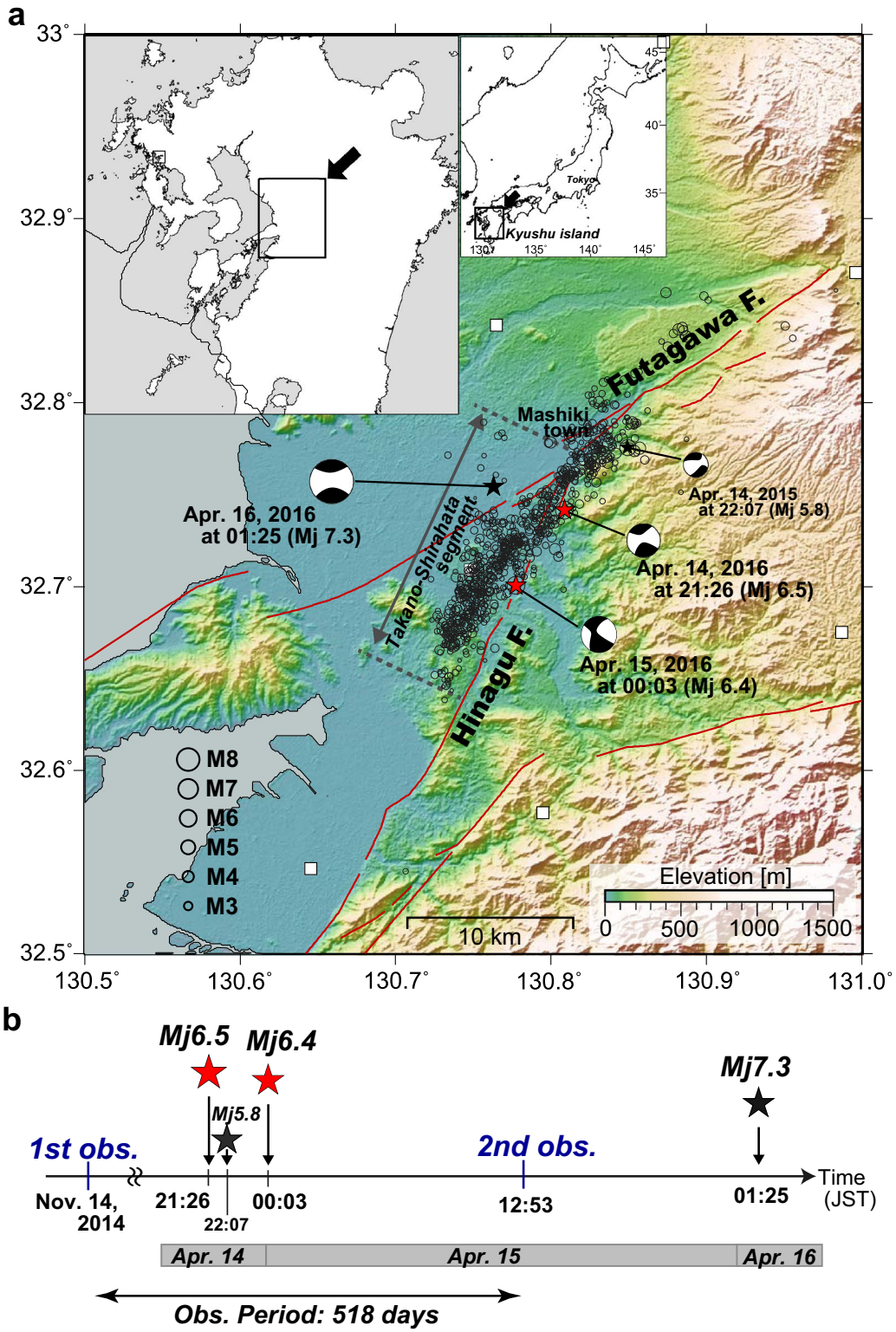

Fig. 1 **a** Tectonic setting of Kumamoto area. *Red stars* indicate epicenters of M_j 6.5 and M_j 6.4 events. *Black star* indicates the M_j 7.3 main shock. *Open circles* stand for epicenters from just after the M_j 6.5 event until the main shock event. *White squares* are GEONET sites. *Red lines* indicate active faults from HERP (2013). Beach ball diagrams are from JMA (2016b). The locations of the source region and Kyushu island are shown in the *inset*. **b** Temporal relationship between SAR observations and relevant earthquakes. The time is Japan Standard Time (JST)

Table 1 Analyzed ALOS-2 images

Date	Time (JST)	Flight Dir	Beam Dir	Obs. Mode	Incidence Angle	Flight Dir	Bp
November 14, 2014	12:53	Des	Left	U	32°	193°	−104 m
April 15, 2016				U			

A letter "U" means stripmap [Fine (3 m)] mode. "Bp" means a perpendicular baseline. The azimuth of the flight direction is measured clockwise from the north

Crustal deformation map

Figure 2 shows the obtained InSAR image. A distinct double-lobe pattern can be clearly identified on the western side of the Hinagu fault zone. The crustal deformation is distributed over an approximately 10 km distance for each concentric fringe. The northern and southern phase changes show slant-range shortening and lengthening with a maximum LOS displacement of 8 and 16 cm, respectively.

Figure 2b shows the MAI result. The cold and warm colors represent the displacement along and opposite to the satellite flight direction, respectively. Although the original MAI result suffers from serious long-wavelength noise (Additional file 1: Fig. S1a), there is a conspicuous phase change showing northward movement on the western side of the Hinagu fault zone. A sharp, linear contrast in displacement, indicated by arrows in the inset of the figure, can be identified along the Hinagu fault. It is highly probable that this sharp phase contrast reflects the fault motion, and its orientation shows the strike of the source fault.

To clearly map the deformation, I applied a Gaussian filter in order to model the long-wavelength noise (Additional file 1: Fig. S1b) and then subtracted the modeled noise from the original MAI result (Additional file 1: Fig. S1c). I have searched the width of Gaussian filter from 10 to 50 km with an interval of 10 km so as to reproduce well the long-wavelength noise by trial and error, and resultantly a width of 30 km was used for the filtering. Figure 2b shows the noise-reduced MAI image. Northward ground movement clearly appears on the western side of the Hinagu fault zone, with maximum movement

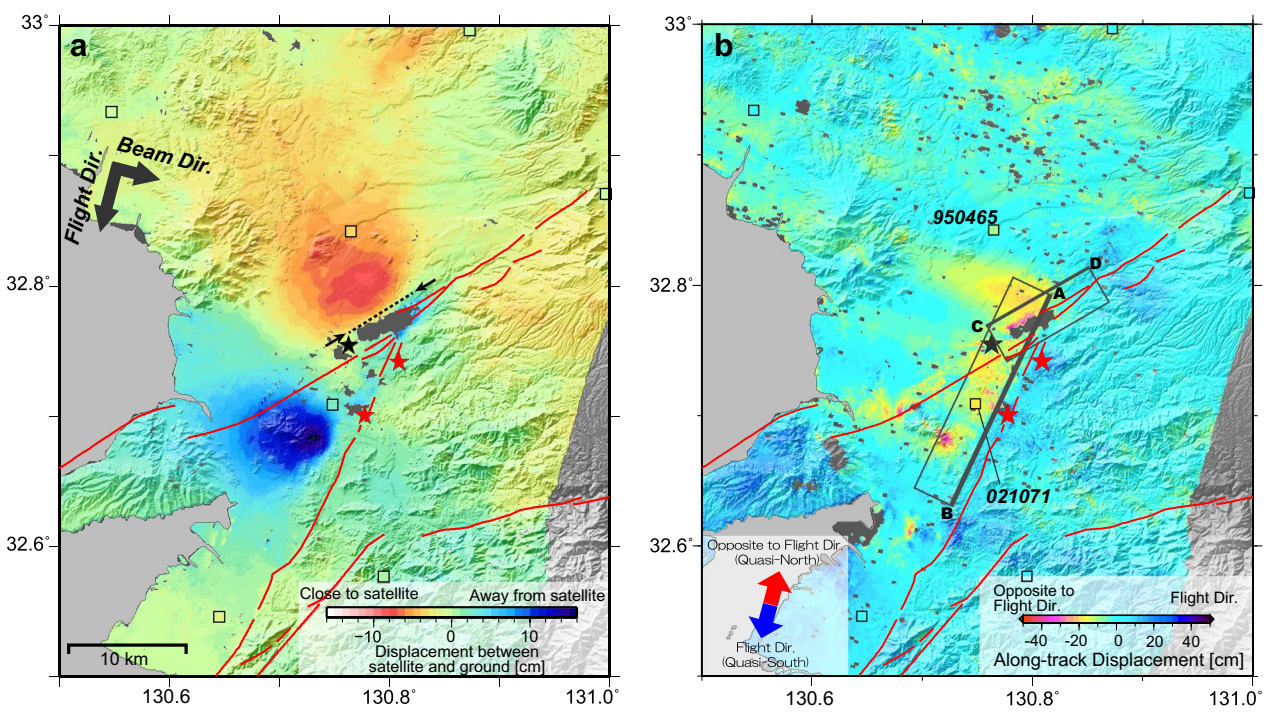

Fig. 2 **a** Cross-track and **b** along-track interferograms by standard InSAR and MAI analyses. They are obtained from the SAR data acquired on November 14, 2014, and April 15, 2016. *Squares* indicate GEONET sites, and their *colors* represent the estimated line-of-sight and azimuth displacements for **a**, **b**, respectively. Both data are unwrapped. The *gray* frames indicate surface projections of the fault planes for modeling (Fig. 3), and the *thick lines* represent the upper edges

of approximately 20 cm. On the other hand, no significant southward movement is shown on the eastern side.

The measurement accuracy of MAI is generally worse than that of InSAR. According to several previous studies, the accuracy of MAI is approximately 10 cm (Bechor and Zebker 2006; Barbot et al. 2008; Jung et al. 2009). To confirm the reliability of the observations, I compared the MAI result to the corresponding GNSS data. The colors of squares in Fig. 2b indicate the displacements converted to the azimuth component at the GEONET sites. The colors of the GNSS site are similar to the background color, suggesting that there is no large difference from GNSS observations. The mean and the standard deviation of residuals between GNSS and MAI results for all stations shown in Fig. 2 are estimated to be 0.4 and 8.7 cm, respectively. The MAI results at GEONET sites 021071 and 950465, which are located in the major deformation area, are −11.1 and −2.7 cm, while the corresponding GNSS-observed displacements are −18.7 and −9.9 cm, respectively. Although a measurement error of ~7 cm remains, it is clear that the large northward movement colored in yellow significantly exceeds the noise level and reflects true crustal deformation.

I further emphasize that local but non-negligible signal can be identified in the junction of the Hinagu and the Futagawa faults where Mashiki town is located. Apart from the two broad deformation signals depicted in Fig. 2a, a significant LOS lengthening signal is locally distributed in and around Mashiki town (Fig. 2a, Additional file 2: Fig. S2). It suggests that this phase change is caused by a different mechanism from the motion on the Hinagu fault responsible for the more widely distributed phase change. This local signal appears to be aligned along the strike of the Futagawa fault. The LOS shortening lobe distributed in the north appears to be oriented somewhat parallel to the strike of the Futagawa fault as indicated by a dotted line in Fig. 2a (Additional file 2: Fig. S2b), suggesting that the responsible fault motion might be related to the Futagawa fault. It is suggested that Mashiki town was subjected to this specific, local deformation.

Fault model

I first constructed a fault model under the assumption of a rectangular fault with a uniform slip in an elastic half-space (Okada 1985). With the knowledge obtained from the InSAR and the MAI data, I assumed two fault planes, of which one runs along the Hinagu fault while the other is beneath Mashiki town along the strike of the Futagawa fault. I estimated the fault model parameters by a simulated annealing method (e.g., Kobayashi et al. 2012). To estimate the individual confidence of inferred parameters, I employed a bootstrap method (Efron 1979). The parameters for the Hinagu fault were searched as below. The obtained displacement field is consistent with a right-lateral motion along the Hinagu fault, and thus, the rake was assumed to be a right-lateral with no constraint on dip-slip orientation. The major displacement is distributed in the western side of the Hinagu fault for both the components, suggesting that the fault has a west-dipping plane. This is why the strike was fixed to be 205°. Other parameters were assigned search ranges of 130.74°–130.80° in longitude, 32.71°–32.78° in latitude, 0–10 km in depth, 0–20 km in length, 0–20 km in width, 0°–90° in dip, and 0–2 m in slip amount, respectively. The given positions are the fault top center. In the same manner, for the local fault beneath Mashiki town, the search ranges were 130.78°–130.81° in longitude, 32.76°–32.79° in latitude, 0–10 km in depth, 0–10 km in length, 0–10 km in width, and 0–2 m in slip amount, respectively. The strike was fixed to be the strike of the Futagawa fault. I here set both the angles of 240° and 60°, meaning that both the north- and south-dipping faults were searched. Neither the dip nor the rake was constrained.

The InSAR and MAI data have ground surface changes over distances of several tens of kilometers, producing too many values to be easily assimilated in a modeling scheme. In order to reduce the number of data for the modeling analysis, I resampled both the InSAR and the MAI data beforehand, using a quadtree decomposition method. Essentially, I followed an algorithm presented by Jónsson et al. (2002). For a given quadrant, if, after removing the mean, the residue is greater than a prescribed threshold, the quadrant is further divided into four new quadrants. I here set the threshold to be 1 and 2 cm for InSAR and MAI data, respectively. This process is iterated until either each block meets the specified criterion or the quadrant reaches a minimum block size, 4×4 and 16×16 pixels for InSAR and MAI, respectively. For the MAI, the area used for the modeling is limited in the proximity of the faults to suppress the effect of the noise. The resampled data are shown in Additional file 3: Fig. S3.

For the weight of inversion, I assigned standard deviations of 1.2 and 5.0 cm for InSAR and MAI data, respectively, which are calculated using phase changes outside of the source region. I additionally utilized GNSS data for the modeling and gave the standard deviations of the time series data during the averaged period for the weight of inversion, on average 0.4, 0.3, and 0.9 cm for E–W, N–S, and up–down components, respectively.

The obtained fault parameters are listed in Table 2. The model is able to reproduce well the observation (Additional file 4: Fig. S4). The dip of the fault beneath Mashiki town is determined to be southward-dipping. Additional file 5; Fig. S5 shows the best solution when the dip is assumed to be north-dipping (Table 3). The

Table 2 Fault parameters for the two-fault model with uniform slips

Fault	Lon (°)	Lat (°)	Depth (km)	Length (km)	Width (km)	Strike (°)	Dip (°)	Rake (°)	Slip (m)	M_w
#1	130.806 (0.007)	32.775 (0.005)	1.2 (0.4)	12.7 (0.7)	6.5 (2.0)	205 –	79.0 (8.7)	176.2 (1.8)	0.9 (0.1)	6.17
#2	130.782 (0.005)	32.773 (0.004)	3.1 (0.6)	4.9 (1.1)	4.1 (1.0)	60 –	69.1 (9.0)	−110.3 (12.1)	0.7 (0.2)	5.68
Total										6.22

Faults #1 and #2 are the Hinagu fault and the local fault beneath Mashiki town, respectively. The units of length, width, and depth are in kilometers; those of dip, strike, and rake are in degrees, and that of slip is in meters. The location of the fault is indicated in the top-left corner. The parenthesized numbers are the standard deviation (1σ)

north-dipping fault also can account for the displacement field well. The root mean squares (RMSs) are estimated to be 1.2 and 1.3 cm for the south- and north-dipping faults, respectively. There is no significant visible difference in fitting between the south- and north-dipping faults, but the Akaike's information criterion (AIC) (Akaike 1974) values support the south-dipping model (AIC = 153.8) rather than the north-dipping one (AIC = 212.7). According to NIED (2016) and Kyushu University (2016), the hypocenters align along a west-dipping orientation in the central part of the Hinagu fault, while in the northern part, where the hypocenter of M_j 6.5 is located, the distribution extends slightly deeper toward the east rather than to the west. Although there is no decisive evidence, the south-dipping fault seems to be the favorable solution.

Next, with the knowledge obtained from the uniform slip model, I constructed a model for the foreshocks to map the detailed slip distribution. The slip distribution model is inferred by a least squares method, following the general procedure of Kobayashi et al. (2012). In the inversion, only the dip-slip and strike-slip components are estimated for each patch. The increase of model parameters gives rise to instability of the solution. To stabilize the solution, I here impose a spatial smoothness constraint on the slip distribution using a Laplacian operator. The relative weight of the constraints is determined by Akaike's Bayesian information criterion (Akaike 1980). For the Hinagu fault, the fault plane was set to a rectangle 20 km long and 20 km wide. The strike angle was set at 205°, so as to be parallel to the Hinagu fault zone. The northern edge of the fault plane is set to be around the junction of the Hinagu fault and the Futagawa fault. For the local fault under Mashiki town, the fault plane was set to a rectangle 10 km long and 10 km wide, and dips to the south with a strike angle of 60°. Both planes are divided into 2 × 2 km squares.

The problem is a nonlinear inversion on a parameter of the dip angle. Here, with the results obtained from the previous modeling, I determined the dip angle by grid searches from 75° to 85° for the Hinagu fault and from 65° to 75° for the local fault with an interval of 5°, for each. The horizontal position is also a linearly unsolved parameter, and thus, I shifted the fault top position westward from [130.820°E, 32.795°N] with an interval of 0.005° for the Hinagu fault. Also for the local fault in the Mashiki town, I shifted the position northward from [130.760°E, 32.760°N] with an interval of 0.005°. The fault top position was fixed to a depth of 0.5 km below the surface by trial and error. The parameter set giving the minimum residuals was adopted as the optimal solution.

Figure 3a, b shows the estimated slip distribution for the Hinagu fault and the local fault beneath Mashiki, respectively. The optimal dip angle and the left top position of the fault plane are 80° and 130.815° E, 32.795°N for the Hinagu fault and 70° and 130.760° E, 32.770°N for the local fault, respectively, indicated by the frame in Fig. 2b. Almost pure dextral movement is predominant over the fault plane for the Hinagu fault, while almost pure normal slip is estimated for the local fault. Figure 4a, b shows the calculated LOS displacement predicted from the constructed model and the residual between

Table 3 Same as Table 2 but for the model assuming that the fault of #2 is dipping north

Fault	Lon (°)	Lat (°)	Depth (km)	Length (km)	Width (km)	Strike (°)	Dip (°)	Rake (°)	Slip (m)	M_w
#1	130.807 (0.007)	32.771 (0.005)	1.0 (0.6)	11.5 (0.9)	8.2 (3.1)	205 –	76.3 (5.0)	173.9 (2.6)	0.8 (0.3)	6.17
#2	130.837 (0.005)	32.776 (0.005)	1.3 (0.8)	6.2 (1.1)	4.5 (1.1)	240 –	41.4 (14.7)	−97.1 (36.3)	0.3 (0.2)	5.53
Total										6.20

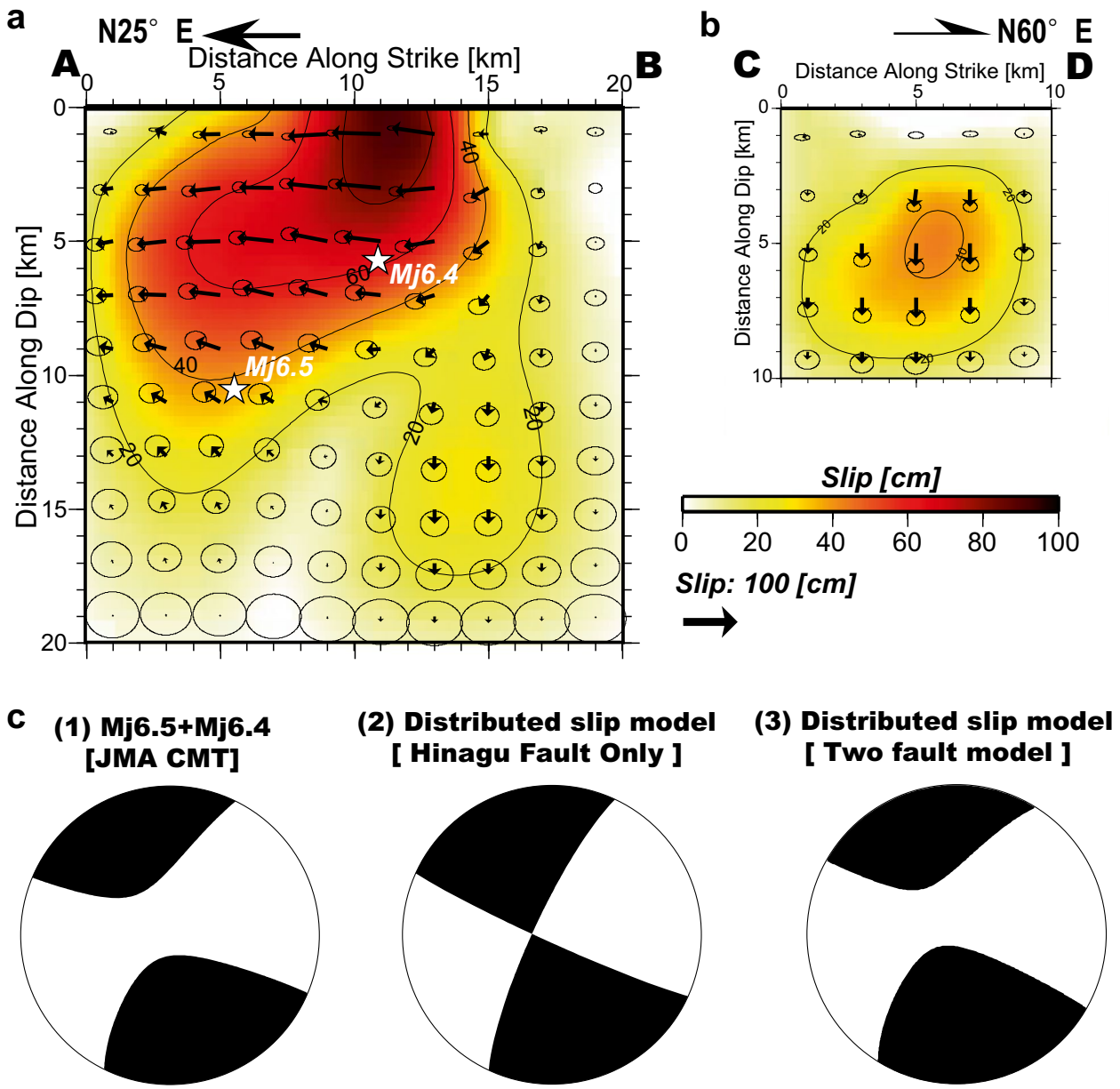

Fig. 3 Slip distribution models for **a** the Hinagu fault and **b** the local fault beneath Mashiki town. The *arrows* show slip vectors of the hanging wall. The contour interval is 20 cm. *Stars* represent hypocenters projected on the fault plane for M_j 6.5 and M_j 6.4 events. The position of the fault plane is shown in Fig. 2. *Error ellipses* show 68% confidence levels. **c** Focal mechanism estimated from moment tensor components. (1) Focal mechanism for both M_j 6.5 and M_j 6.4 events. The moment tensors determined by JMA (2016b) are used. (2) Focal mechanism estimated from distributed slip model of the Hinagu fault alone. (3) Focal mechanism estimated from distributed slip models of both the Hinagu fault and the local fault beneath Mashiki town. The mechanisms are estimated assuming a point source

the observations and the calculations. The model is able to reproduce well the two main lobes of the InSAR data and the locally distributed LOS lengthening signal in and around Mashiki town. The model also can account for the azimuth displacement field in which approximately northward movement occurs on the western side of the Hinagu fault (Fig. 4c). The residual is reduced to the level of the background noise level (Fig. 4d). The GNSS data are also reproduced well by the constructed model (Fig. 4e). The RMS of the residuals is estimated to be 0.9 cm. The seismic moments are estimated to be 3.31×10^{18} Nm (M_w 6.28) for the Hinagu fault and 6.11×10^{17} Nm (M_w 5.79) for the local fault, adding up to 3.92×10^{18} Nm (M_w 6.33), assuming a rigidity of 30 GPa.

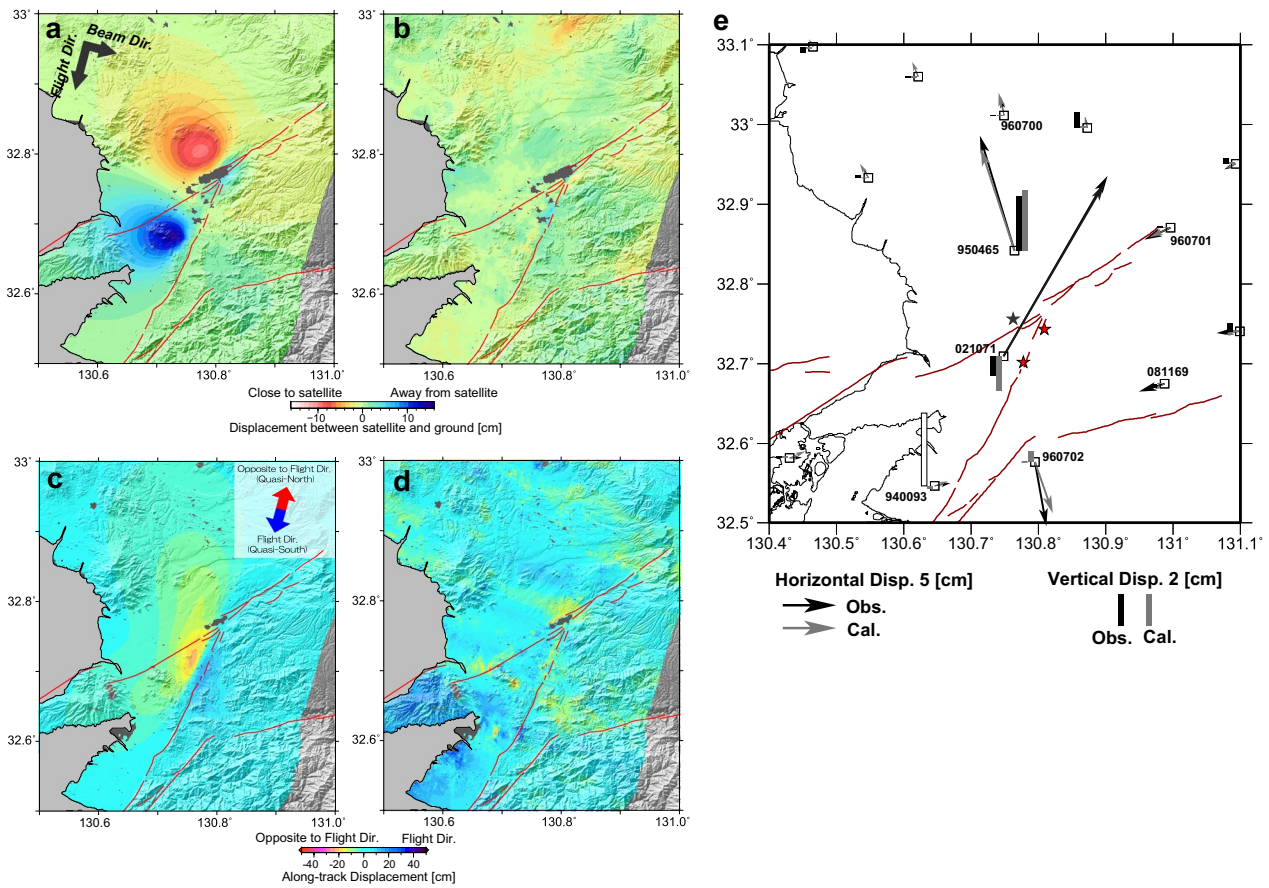

Fig. 4 **a** LOS displacement field calculated from the constructed distributed slip model. **b** Residual between the observations (Fig. 2a) and the calculations (**a**). **c**, **d** Same as **a**, **b**, respectively, but for MAI results. **e** Coseismic displacements at GEONET sites. *Arrows* and *bars* represent *horizontal* and *vertical* displacements, respectively. *Black* and *gray* represent the observed and model-predicted displacements, respectively. The *vertical* component of site 940093, indicated by a *white-colored bar*, is not used for the modeling

According to the results of JMA, NIED, and Global CMT (GCMT) solutions, the combined seismic moments of M_j 6.5 and M_j 6.4 events are 3.45 $\times$ 10^{18} Nm (M_w 6.29), 2.80 $\times$ 10^{18} Nm (M_w 6.23), and 3.32 $\times$ 10^{18} Nm (M_w 6.28), respectively. The obtained result is in good agreement with the seismic analyses.

The slip on the Hinagu fault significantly extends down to around 10 km depth and reaches around the junction of the Futagawa and the Hinagu faults. A large slip concentrates near the ground surface and extends downward to the north. According to the JMA catalog, the hypocenters for the M_j 6.5 and the M_j 6.4 events are located in the northern part of the Hinagu fault at 11 ($\pm$0.9) km depth and at 6 ($\pm$1.6) km depth in the southern part, respectively (Fig. 3a). The InSAR data consist of the displacements produced primarily by these two events (Fig. 1b); thus, the distributed slip model should encompass the source properties of both events. Taking the spatial relationship into consideration, this may suggest that the northern deep slip and the southern shallow slip correspond to the M_j 6.5 and the M_j 6.4 events, respectively. InSAR analysis cannot further separate the individual crustal deformation due to its poor temporal resolution. The locations where the main slips of each event occurred might be provided by kinematic GNSS data due to its high sampling rate (Kawamoto et al. 2016).

Discussion

Local normal fault motion: why was the damage so large in Mashiki?

One of the notable points is that the InSAR observation has successfully detected the locally distributed ground motion in and around Mashiki town owing to the high spatial resolution. And it should be noted that the favorable fault model producing the deformation is not right-lateral motion but normal faulting, which is in good agreement with the fact that earthquakes with normal fault motions have occurred in this area in the

Kumamoto earthquake sequence (Kyushu University 2016). The spatial proximity with Mashiki town strongly implies that this normal fault motion could be responsible for the damage concentrated within the town. To further inform this discussion, it is vital to know when the fault slip occurred. One of the possibilities is that it occurred simultaneously with the M_j 6.5 event. Here, I focus on the focal mechanism. The striking point for the M_j 6.5 event is that a significant non-double couple component is included in the JMA focal mechanisms (Fig. 1). The non-double couple component can be identified also in other CMT solutions (GCMT 2016; USGS 2016). It implies that the rupture cannot be accounted for by a simple fault motion on a single fault plane; instead, it is composed of a complicated slip distribution on one fault plane or composite fault motions by multiple fault planes.

In this context, I calculated the total moment tensor components using the estimated parameters for all patches of the distributed slip model of the Hinagu fault alone and made a beach ball plot [Fig. 3c(2)] (Lay and Wallace 1995). For the estimate, I assumed a point source. The beach ball shows simple right-lateral motion, which consists of a double couple component. Hence, it indicates that a different rupture by another fault is necessary. Here, recall the local fault producing the phase change in Mashiki town. Incorporating the contribution of normal fault motion into the estimate of moment tensor, a significant non-double couple component appears [Fig. 3c(3)]. InSAR data include the effects of both the M_j 6.5 and M_j 6.4 events, and thus, I calculated a seismically estimated focal mechanism combining both the events, using moment tensor components determined by JMA (2016b) [Fig. 3a(1)]. It is striking that the focal mechanism predicted by both the Hinagu fault and the local normal faulting has a considerable resemblance to that determined by the seismic analysis. This pronounced consistency strongly suggests that normal faulting did occur beneath Mashiki town, away from the main right-lateral rupture. The normal fault rupture may be one of the primary causes for locally increased ground shaking and damage to Mashiki town.

Localized normal faulting can effectively explain both the InSAR and seismic data; however, careful interpretation is necessary because there may be other reasons for the local phase change. One of the possibilities is an M_j 5.8 event that occurred at 22:07 on April 14, whose hypocenter was located near the local phase change area (Fig. 1). Furthermore, according to the JMA catalog, the strike and dip are concordant with the estimated south-dipping fault model, and the moment magnitude is also similar. However, the focal depth is seismically estimated to be 8 (±1.2) km. If this is true, it cannot produce significant ground displacement with seismic energy of M_j 5.8 (M_w 5.4). Shallow fault slip is essential to produce the observed ground displacement; hence, the link to the M_j 5.8 event seems unlikely but cannot be rejected entirely.

Another possibility is an effect of liquefaction. It is known that liquefaction induces ground subsidence and can be sometimes detected by InSAR (Ishitsuka et al. 2012). Liquefaction occurred in some parts of Mashiki town during the earthquake series, yet the timing of liquefaction does not appear to be known. Therefore, this possibility can also not be excluded.

The existence of a shallow local fault is a reasonable hypothesis for why Mashiki town suffered such locally concentrated damage in spite of the moderate-sized earthquake and why a significant non-double couple component is included in the M_j 6.5 event. This investigation, however, is far from exhaustive due to limited observations. At this stage, I claim only that this provisional model is consistent with some facts. I stress that reinvestigation assuming such a local fault rupture beneath Mashiki town is essential to further develop our understanding of the Kumamoto earthquake in other study fields.

The effect on the M_j 7.3 event

Finally, I will briefly discuss an effect on the main shock due to a static stress change. The crust in the proximity of the foreshock rupture fault should be subjected to a strong stress change, which presumably culminates in promotion of the main shock. To test this idea quantitatively, I evaluated ΔCFF values (King et al. 1994) at the epicenter of the M_j7.3 event. I assumed the focal mechanism of initial motion for the M_j 7. 3 event as a receiver mechanism (JMA 2016a). I then evaluated the stress change pattern for an effective coefficient of friction μ ranging from 0.2 to 0.7 and a depth from 1 to 20 km. The estimated ΔCFF is shown in Additional file 6: Fig. S6a. To further evaluate sensitivity to horizontal position errors of the hypocenter, I shifted the epicenter to four directions (northward, southward, westward, and eastward) and calculated ΔCFF for each case in the same manner. The standard deviation of the hypocenter is 260 m in latitude and 310 m in longitude, respectively, and thus, I here shifted to 0.5 km, equivalent to 2σ, in each orientation (Additional file 6: Fig S6b–e). Warm and cold colors represent positive and negative signs, signifying facilitated or suppressed fault slip, respectively. In and around the depth of the hypocenter (12 km), the ΔCFF values tend to be positive with higher μ and negative with lower μ. Although I cannot definitively conclude that the main shock was triggered by the static stress change, it seems possible that the foreshocks promoted the main shock. On the other hand, the ΔCFF values have positive signs deeper than 17 km for any μ, suggesting that fault slips

are robustly promoted at depth near the lower edge of the so-called seismogenic zone. Also in other cases, it can be identified that a fault slip tends to be promoted in the deep rather than the shallow (Additional file 6: Fig. S6b–e) although there are slight differences at some points. Of course, care must be taken with these estimates because the source and the receiver faults are near to one another and thus the estimate is sensitive to the position and the given slip mechanism. To clarify this, further study on the rupture for the main shock is vital for developing our understanding of this issue in the future.

Conclusions

By applying InSAR and MAI techniques to ALOS-2 data, I have successfully retrieved the crustal deformation associated with two foreshocks (M_j 6.5 and M_j 6.4) of the 2016 Kumamoto earthquake and obtained the source properties. The findings are conceptually summarized in Fig. 5. The following conclusions were derived from the analyses.

1. A major displacement field in LOS and azimuth components is distributed on the western side of the Hinagu fault with the displacement exceeding 15 cm.
2. A locally distributed ground displacement which appears along the strike of the Futagawa fault is clearly identified in and around Mashiki town, suggesting that a different local fault slip is also partially responsible for the foreshocks.
3. The constructed model shows almost pure right-lateral fault motion with M_w 6.28 for the Hinagu fault. The slip in the north significantly extends down to around 10 km depth, while in the south a large slip concentrates near the ground surface, perhaps corre-

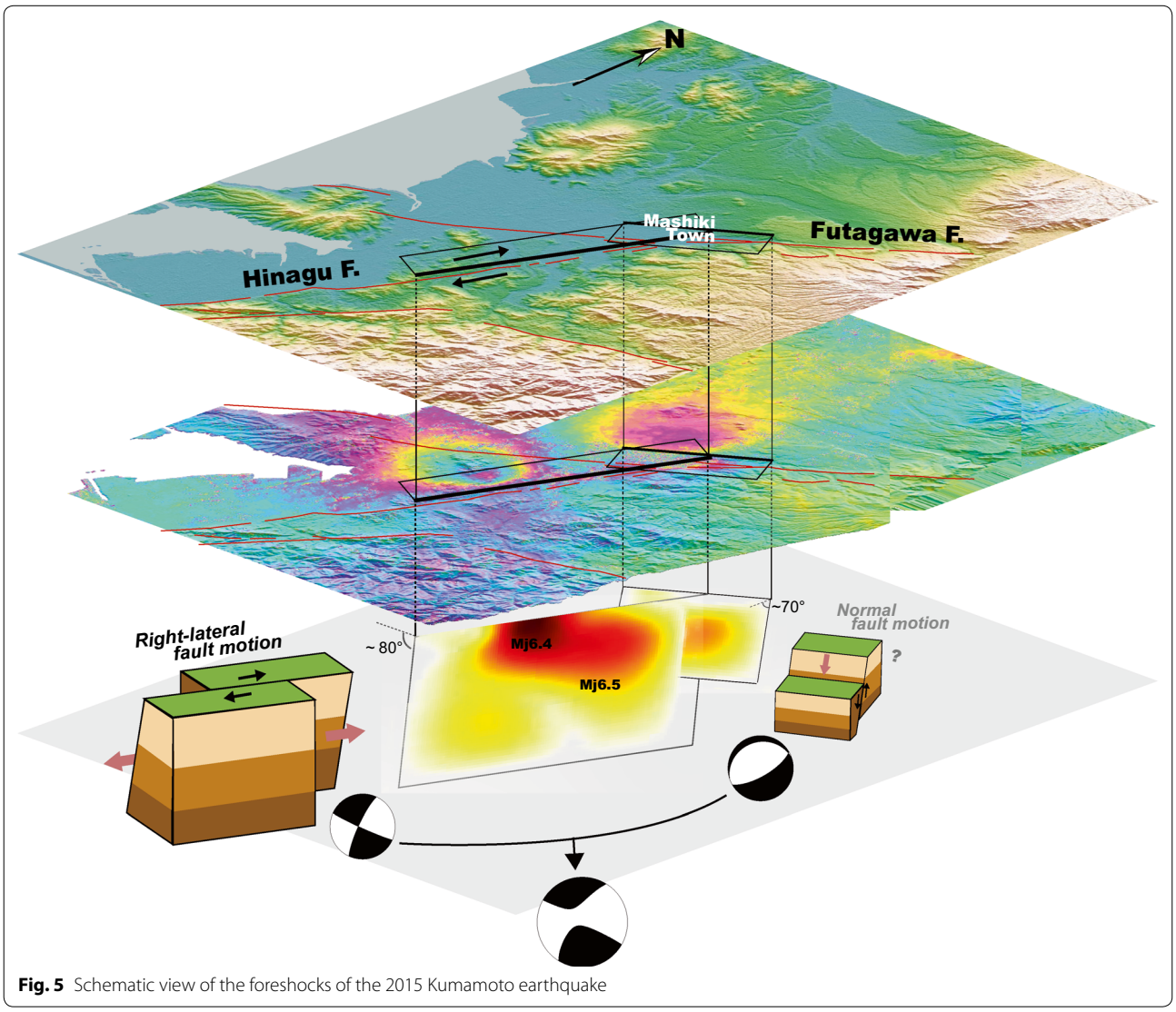

Fig. 5 Schematic view of the foreshocks of the 2015 Kumamoto earthquake

sponding to the M_j 6.5 and the M_j 6.4 events, respectively. On the other hand, almost pure normal fault motion with M_w 5.79 is inferred for the local fault beneath Mashiki town.

4. Although the inferred slip distribution for the Hinagu fault alone does not have a significant non-double couple component inferred from seismic analyses, if incorporating the contribution from normal faulting, the focal mechanism bears a great resemblance to the seismically estimated mechanism. This might suggest that the normal faulting occurred simultaneously with the M_j 6.5 event, which locally amplified the damage to Mashiki town.

Additional files

Additional file 1: Fig. S1. MAI analysis results. **a** Original MAI result. Note that the *color scale* for the inset has been changed to make the phase boundary clearer. **b** Long-wavelength-noise model constructed by Gaussian filtering. **c** Noise-reduced MAI image.

Additional file 2: Fig. S2. **a** Wrapped InSAR image. Squares indicate GEONET sites, and their *colors* represent the estimated line-of-sight displacements. **b** Enlarged views of wrapped InSAR results. LOS lengthening displacement is locally distributed in and around Mashiki town. The LOS shortening lobe distributed in the north appears to be flattened somewhat parallel to the strike of the Futagawa fault as indicated by a *dotted line*.

Additional file 3: Fig. S3. Downsampled data used in the modeling for **a** InSAR and **b** MAI, respectively.

Additional file 4: Fig. S4. **a** LOS displacement field calculated from the fault model assuming *two rectangle* fault planes with uniform slips. The frames indicate surface projections of the obtained fault planes for modeling and the *thick line* represents the upper edges. **b** Residual between the observations (Fig. 2a) and the calculations (**a**). **c**, **d** Same as **a**, **b**, respectively, but for the MAI data. **e** Coseismic displacements at GEONET sites. *Arrows* and *bars* represent horizontal and vertical displacements, respectively. *Black* and *gray* represent the observed and model-predicted displacements, respectively.

Additional file 5: Fig. S5. Same as Fig. S4 but for the model assuming the north-dipping fault plane for the local fault beneath Mashiki town.

Additional file 6: Fig. S6. ΔCFF distributions as a function of depth and effective coefficient of friction. **a** ΔCFF calculated using the epicenter position determined by JMA as a receiver fault. **b** ΔCFF calculated using the position shifted 0.5 km northward from the epicenter. **c** Same as **b** but for 0.5 km southward shift. **d** Same as **b** but for 0.5 km westward shift. **e** Same as **b** but for 0.5 km eastward shift.

Acknowledgements
ALOS-2 data were provided from the Earthquake Working Group under a cooperative research contract with JAXA (Japan Aerospace Exploration Agency). The ownership of ALOS-2 data belongs to JAXA. Generic Mapping Tools (GMT) provided by Wessel and Smith (1998) were used to construct the figures. Hypocenter data processed by the Japan Meteorological Agency (JMA) were used. I thank reviewers (Dr. R. Walters and the anonymous reviewers) and the editor for their helpful comments to improve our manuscript.

Competing interests
The author declares that he has no competing interests.

Received: 5 July 2016 Accepted: 20 December 2016
Published online: 03 January 2017

References

Akaike H (1974) A new look at the statistical model identification. IEEE Trans Autom Control 19:716–723
Akaike H (1980) Likelihood and the Bayes procedure. In: Bernardo JM, DeGroot MH, Lindley DV, Smith AFM (eds) Bayesian Statistics. University Press, Valencia
Asano K, Iwata T (2016) Source rupture processes of the foreshock and mainshock in the 2016 Kumamoto earthquake sequence estimated from the kinematic waveform inversion of strong motion data. Earth Planets Space 68:147. doi:10.1186/s40623-016-0519-9
Barbot S, Hamiel Y, Fialko Y (2008) Space geodetic investigation of the coseismic and postseismic deformation due to the 2003 M(w)7.2 Altai earthquake: implications for the local lithospheric rheology. J Geophys Res. doi:10.1029/2007jb005063
Bechor NBD, Zebker HA (2006) Measuring two-dimensional movements using a single InSAR pair. Geophys Res Lett 33:L16311. doi:10.1029/2006GL026883
Efron B (1979) Bootstrap methods: another look at the jackknife. Ann Statis 7:1–26
Fujiwara S, Tobita M (1999) SAR interferometry techniques for precise surface change detection. J Geod Soc Jpn 45:283–295 **(in Japanese with English abstract)**
Fujiwara S, Tobita M, Murakami M, Nakagawa H, Rosen PA (1999) Baseline determination and correction of atmospheric delay induced by topography of SAR interferometry for precise surface change detection. J Geod Soc Jpn 45:315–325 **(in Japanese with English abstract)**
Global Centroid Moment Tensor Catalog (2016) 201604141226A KYUSHU, Japan. http://www.globalcmt.org. Accessed 22 Nov 2016
Goldstein R, Werner C (1998) Radar interferogram filtering for geophysical application. Geophys Res Lett 25:4035–4038
Headquarters for Earthquake Research Promotion (2013) Evaluation of active faults to date. http://jishin.go.jp/main/chousa/katsudansou_pdf/93_futagawa_hinagu_2.pdf **(in Japanese)**
Ishitsuka K, Tsuji T, Matsuoka T (2012) Detection and mapping of soil liquefaction in the 2011 Tohoku earthquake using SAR interferometry. Earth Planets Space 64:1267–1276. doi:10.5047/eps.2012.11.002
Japan Meteorological Agency (2016a) Focal mechanism catalog using initial motion. http://www.data.jma.go.jp/svd/eqev/data/mech/ini/mc201604.html. Accessed 17 June 2016 **(in Japanese)**
Japan Meteorological Agency (2016b) CMT catalog. http://www.data.jma.go.jp/svd/eqev/data/mech/cmt/cmt201604.html. Accessed 17 June 2016. **(in Japanese)**
Jónsson S, Zebker H, Segall P, Amelung F (2002) Fault slip distribution of the 1999 M_w 7.1 Hector Mine, California, earthquake, estimated from satellite radar and GNSS measurements. Bull Seismol Soc Am 92:1377–1389
Jung HS, Won JS, Kim SW (2009) An improvement of the performance of multiple-aperture SAR interferometry (MAI). IEEE Trans Geosci Remote Sens 47:2859–2869
Kawamoto S, Hiyama Y, Ohta Y, Nishimura T (2016) First result from the GEONET real-time analysis system (REGARD): the case of the 2016 Kumamoto earthquakes. Earth Planets Space 68:190. doi:10.1186/s40623-016-0564-4
King GCP, Stein RS, Lin J (1994) Static stress changes and the triggering of earthquakes. Bull Seismol Soc Am 84:935–953
Kobayashi T, Takada Y, Furuya M, Murakami M (2009) Locations and types of ruptures involved in the 2008 Sichuan Earthquake inferred from SAR image matching. Geophys Res Lett. doi:10.1029/2008GL036907
Kobayashi T, Tobita M, Koarai M, Okatani T, Suzuki A, Noguchi Y, Yamanaka M, Miyahara B (2012) InSAR-derived crustal deformation and fault models of normal faulting earthquake (M_j7.0) in Fukushima-Hamadori area. Earth Planets Space 64:1209–1221. doi:10.5047/eps.2012.08.015
Kobayashi T, Ishimoto M, Tobita M, Yarai H (2014) A tool for reduction of atmosphere-related noises included in an InSAR image, incorporating a numerical weather model. Bull GSI 125:31–38 **(in Japanese)**
Kyushu University (2016) Characteristic of hypocentral distribution. http://cais.gsi.go.jp/YOCHIREN/activity/211/image211/031-034.pdf. Accessed 17 June 2016 **(in Japanese)**
Lay T, Wallace TC (1995) Modern global seismology. Academic Press, San Diego
Michel R, Avouac JP, Taboury J (1999) Measuring ground displacements from SAR amplitude images: application to the Landers earthquake. Geophys Res Lett 26:875–878

Nakagawa H, Toyofuku T, Kotani K, Miyahara B, Iwashita C, Kawamoto S, Hatanaka Y, Munekane H, Ishimoto M, Yutsudo T, Ishikura N, Sugawara Y (2009) Development and validation of GEONET new analysis strategy (Version 4). J. Geogr. Surv. Inst. 118:1–8 **(in Japanese)**

National Research Institute for Earth Science and Disaster Resilience (2016) Evaluation of earthquake in Kumamoto region, Kumamoto Prefecture on April 16, 2016. http://www.jishin.go.jp/main/chousa/16apr_kumamoto2/p05-e.htm. Accessed 17 June 2016 **(in Japanese)**

Okada Y (1985) Surface deformation due to shear and tensile faults in a halfspace. Bull Seismol Soc Am 75:1135–1154

Scheiber R, Moreira A (2000) Coregistration of interferometric SAR images using spectral diversity. IEEE Trans Geosci Remote Sens 38:2179–2191. doi:10.1109/36.868876

US Geological Survey (2016) M6.2—3 km W of Kumamoto-shi, Japan. http://earthquake.usgs.gov/earthquakes/eventpage/us20005hzn#moment-tensor. Accessed 22 Nov 2016

Tobita M (2003) Development of SAR interferometry analysis and its application to crustal deformation study. J Geod Soc Jpn 49:1–23 **(in Japanese with English abstract)**

Tobita M, Fujiwara S, Murakami M, Nakagawa H, Rosen PA (1999) Accurate offset estimation between two SLC images for SAR interferometry. J Geod Soc Jpn 45:297–314 **(in Japanese with English abstract)**

Tobita M, Munekane H, Matsuzaka S, Kato M, Yarai H, Murakami M, Fujiwara S, Nakagawa H, Ozawa T (2005) Studies on InSAR data processing technique. Bull GSI 106:37–49 **(in Japanese)**

Wegmüller U, Werner CL (1997) Gamma SAR processor and interferometry software. In: Proceedings of the 3rd ERS symposium, vol SP-414. ESA, Florence, pp 1686–1692

Wessel P, Smith WH (1998) New, improved version of generic mapping tools released. EOS Trans AGU 79:579